ELSEVIER

Biophysical Chemistry 68 (1997) 189–205

Biophysical Chemistry

Electron transfer and electronic energy relaxation under high hydrostatic pressure

Arvi Freiberg *, Aleksandr Ellervee, Märt Tars, Kõu Timpmann, Arlentin Laisaar

Institute of Physics, Riia 142, EE2400 Tartu, Estonia

Received 2 January 1997; revised 20 March 1997; accepted 20 March 1997

Abstract

The following question has been addressed in the present work. How external high (up to 8 kbar) hydrostatic pressure acts on photoinduced intramolecular electron transfer and on exciton relaxation processes? Unlike phenomena, as they are, have been studied in different systems: electron transfer in an artificial Zn-porphyrin–pyromellitimide (ZnP–PM) supramolecular electron donor–acceptor complex dissolved in toluene measured at room temperature; exciton relaxation in a natural photosynthetic antenna protein called FMO protein measured at low temperatures, between 4 and 100 K. Spectrally selective picosecond time-resolved emission technique has been used to detect pressure-induced changes in the systems. The following conclusions have been drawn from the electron transfer study: (i) External pressure may serve as a potential and sensitive tool not only to study, but also to control and tune elementary chemical reactions in solvents; (ii) Depending on the system parameters, pressure can both accelerate and inhibit electron transfer reactions; (iii) If competing pathways of the reaction are available, pressure can probably change the branching ratio between the pathways; (iv) The classical nonadiabatic electron transfer theory describes well the phenomena in the ZnP–PM complex, assuming that the driving force or/and reorganisation energy depend linearly on pressure; (v) A decrease in the ZnP–PM donor-acceptor distance under pressure exerts a minor effect on the electron transfer rate. The effect of pressure on the FMO protein exciton relaxation dynamics at low temperatures has been found marginal. This may probably be explained by a unique structure of the protein [D.E. Trondrud, M.F. Schmid, B.W. Matthews, J. Mol. Biol. 188 (1986) p. 443; Y.-F. Li, W. Zhou, E. Blankenship, J.P. Allen, J. Mol. Biol., submitted]. A barrel made of low compressibility β-sheets may, like a diving bell, effectively screen internal bacteriochlorophyll *a* molecules from external influence of high pressure. The origin of the observed slow pico = and subnanosecond dynamics of the excitons at the exciton band bottom remains open. The phenomenon may be due to weak coupling of phonons to the exciton states or/and to low density of the relevant low-frequency ($\approx 50\ cm^{-1}$) phonons. Exciton solvation in the surrounding protein and water–glycerol matrix may also contribute to this effect. Drastic changes of spectral, kinetic and dynamic properties have been observed due to protein denaturation, if the protein was compressed at room temperature and then cooled down, as compared to the samples, first cooled and then pressurised. © 1997 Elsevier Science B.V.

Keywords: High pressure; Electron transfer; Energy relaxation; Picosecond fluorescence; Pigment–protein complexes; Photosynthesis

1. Introduction

Electron transfer (ET) and excited electronic state energy relaxation (ER) play a major role in chem-

* Corresponding author. Tel.: +372-7-383024; fax: +372-7-383033; e-mail: freiberg@park.tartu.ee

PII S0301-4622(97)00046-X

istry and biology, notably in photosynthesis. Both for cognitive reasons and for development of practical molecular electronics devices, the underlying physical mechanisms should be understood in detail. To gain a proper understanding of these processes, a wide range of equilibrium and dynamical effects need to be characterised.

There are two commonly used experimental approaches to study various aspects of ET and ER: by changing the chemical composition of the solvent and by varying the temperature. Although important results have been obtained, the quantitative understanding of the ET and ER kinetics and dynamics is still rather limited, partly because of serious limitations these methods have. Temperature causes simultaneous changes in volume and thermal energy that are difficult to separate. Changes in the solvent chemical composition are discontinuous and also alter many bulk solvent physical properties (density, viscosity, dielectric susceptibility) at the same time. This motivates the search for complementary experimental approaches.

Pressure as another universal thermodynamic variable may offer an attractive alternative. Continuous tuning of the properties of molecular matter over a wide range, without changing its structure and chemical identity, can be achieved in a controlled manner. Yet, as with temperature, the response of the matter to increasing pressure is presumably complex. In a rather broad sense, pressure effects can be divided into equilibrium or static effects and dynamic effects. The most important static effect is change of average intermolecular distances resulting in alteration of ground- and excited-state free energy surfaces of the dynamic system under study. Dynamic effects are due to modification of the solute-solvent system relaxation characteristics under pressure.

In the first part of the present work (Sections 3.1, 3.2, 4.1 and 4.2), we will demonstrate that external pressures in the kilobar range may serve as a potential and sensitive tool not only to study, but also to control and tune elementary chemical reactions in solutions. As an example, pressure dependence of the photoinduced intramolecular ET in a donor–acceptor complex dissolved in toluene has been investigated.

The supramolecular complex under study consists of the zinc *meso*-tripentylmonophenylporphyrin (ZnP) electron donor and the pyromellitimide (PM) electron acceptor. The donor molecule is covalently bridged via a phenyl side-ring to the acceptor molecule yielding a structurally rigid supermolecule with the centre-to-centre donor–acceptor distance of about 1.5 nm (Fig. 1). The porphyrin-based donor–acceptor complex was favoured because of the central role of the porphyrin ring system in photosynthesis, oxygen transport, and in biological oxidation and reduction processes.

There are essential advantages to study intramolecular ET as contrasted to intermolecular ET between weakly (non-covalently) coupled donor and acceptor molecules. The first advantage is that ET rate can be monitored directly, without interference with the diffusion of donor and acceptor components. The second advantage is that most of the ET rate-limiting parameters, such as donor–acceptor separation, relative orientation of donor and acceptor parts, driving force, and reorganisation energy, can be reasonably well controlled by modern chemical design procedures. Notice, that in natural biomolecular systems (e.g., in the photosynthetic reaction centre proteins), the ET cofactors are fixed in certain (favourable) positions by the rigid framework of the protein backbone.

The specific system has been selected since the driving force and reorganisation energy for the ET reaction are known and they have relatively close values at normal pressure [1]. In this case, the ET rate is expected to be near to its maximum, which makes it easier to compete with other, uninteresting

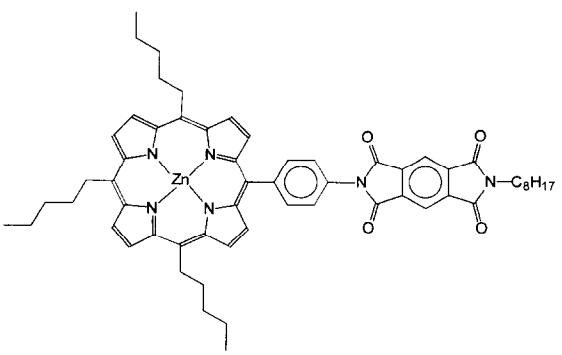

Fig. 1. Molecular structure of the ZnP–PM complex.

in the context of the present work, excited state quenching processes (intersystem crossing, internal conversion, and radiative decay). Also, at the maximum, the derivative of ET rate reverses (pressure in our case) over perturbation with respect to a perturbing factor, its sign giving an additional chance to discriminate weak effects.

Although the pressure studies of the electron donor–acceptor complexes, including reaction centre proteins, have a relatively long history [2–9], the underlying reaction mechanisms have remained mostly unexplored. Both acceleration and deceleration of ET rate with increasing pressure have been observed for different reactions.

In the second part of the work (Sections 3.3, 3.4 and 4.3), we will describe the influence of hydrostatic pressure on the ER dynamics in a photosynthetic antenna bacteriochlorophyll *a*-protein complex called FMO protein (after the names of the pioneer structure investigators Fenna, Matthews, and Olson).

In the green sulphur photosynthetic bacteria, the FMO protein plays a double role: as an antenna for collecting the light energy and as a mediator of light excitations between the extra-membrane chlorosome antenna and the cell membrane (for a recent review, see [10]). The FMO protein structure is presently known at about 0.2 nm resolution [11,12]. It consists of three identical subunits related by a 3-fold axis of crystallographic symmetry. Each subunit encloses seven irregularly spaced bacteriochlorophyll *a* (Bchl) molecules. The distances between neighbouring Bchls in a subunit vary between 0.4 and 1.1 nm, and the distance between Bchls from different subunits exceeds 2 nm. The FMO protein is unique in having a fine-structured Bchl Q_y exciton [13–15] absorption spectrum at low temperatures ($T \leq 150$ K).

Recently, evidence has been obtained for a pico-nanosecond ER process via time-dependent red-shift and broadening of the exciton emission spectrum at 6 K [16,17]. This relaxation is slow compared to the major inter-exciton state relaxation within the protein monomer, which has been proven [17] to take less than a picosecond, but fast compared to the usually observed micro-millisecond time–domain solvation dynamics of the protein backbone. Two nonexclusive interpretations to this effect have been proposed [17]. The phenomenon may be due to ultrafast exciton solvation in the surrounding protein and water–glycerol matrix. It may also result from a slow scattering of phonons from closely spaced exciton states, which are due to weak interactions between Bchl molecules belonging to different monomers in the protein trimer [14,15,18].

Here, we will further explore these questions by varying pressure (between 1 atm and 7 kbar) and temperature (between 6 K and 80 K). In the literature, there are only a couple of works (one from our laboratory) devoted to the steady-state optical absorption [19] and hole-burning spectroscopy [20] of FMO protein-bound pigments under high pressure. Observed was a relatively small and linear (about -12 cm^{-1}/kbar at 55 K [19]) red-shift of the absorption spectrum, presumably due to changes in dispersive interaction between the Bchl molecules and the protein surroundings.

How a complicated system, like the antenna complex under study, would react on high pressure in the kilobar range, is not easy to predict. Notice, for comparison, that pressure at the bottom of the deepest sea is about 1.1 kbar. Among the possible consequences are: change of resonant coupling between the Bchl molecules; modification of the nonresonant (dispersive) coupling between the pigment molecules and their protein surroundings; transformation of the protein conformational states, finally leading to denaturation of the protein. Monomeric proteins usually denaturation in the pressure range from 4 to 8 kbar, whereas large protein oligomers may suffer dissociation already at 1–2 kbar [21,22]. This behaviour can be understood, considering the amount of compression work W per molecule:

$$W \approx \kappa_T v p^2 \qquad (1)$$

Eq. (1) is valid, if $\kappa_T p \ll 1$. κ_T is the isothermal compressibility, v is the molecular volume, p is the applied pressure. It is easy to check that at $p = 1$ kbar, $v \geq 100$ nm^3, and $\kappa_T \geq 10^{-5}$ bar^{-1}, W can readily reach energies that hold together protein subunits in the oligomeric protein. A prominent effect of pressure on the room-temperature spectral properties of the FMO protein trimer will be discussed in Section 3.3. In the case of relatively small molecules, like ZnP–PM donor–acceptor complex, the compression energy at pressures used is very small compared to the energy of chemical bonds, and therefore, can safely be viewed as a weak perturbation only.

2. Experimental

2.1. Sample handling

The ZnP–PM complex was synthesised according to the published procedures [1] in the Chemistry Division, Argonne National Laboratory, USA, and kindly provided to us by Dr. M. Wasielewski. The substance was dissolved in toluene to the concentration of 2×10^{-5}M without further purification. Toluene was chosen as a solvent in order to minimise the solvation effects that limit ET rate in many polar solvents (for a recent review, see [23]).

The FMO trimers were isolated from the green photosynthetic sulphur bacteria *Chlorobium tepidum*, as described [24], and kindly supplied to us by Dr. M. Miller (Odense University, Denmark). The protein solution in the 20mM Tris-HCl buffer (pH = 8.0) was diluted with glycerol in a 1:2 volume ratio. This buffer–glycerol mixture ensures a transparent glass formation by cooling down either at atmospheric or high pressure.

2.2. Pressure equipment

Two different setups were used for optical measurements under hydrostatic pressure: one for experiments at room temperature and another, at variable temperatures between 300 K and 2 K.

At room temperature (295 K), the solution under study was contained in a special sample cell having two windows about 2 mm apart with one window fixed and another translationally movable like a piston to adapt the pressure variations. The construction of the sample cell prevented direct contact of the sample with the pressure transmitting medium. The sample cell was mounted in a simple home-made piston-cylinder type high-pressure optical cell. Three 10 mm-thick sapphire windows of 12 mm diameter cover the light port of 4.5 mm aperture and 30° cone angle in window plugs. A portable hydraulic press was exploited to generate pressure up to about 10 kbar inside the cell by pushing down the piston. As a pressure transmitter, various liquids may be utilised. Here, a mixture of glycerol with water was used.

In low-temperature studies, helium gas served as the pressure-transmitting medium (gaseous helium does not freeze up to 14.6 kbar at 77 K). A commercial 15-kbar three-stage gas compressor (UNIPRESS, Poland) was used to generate high pressure. The compressor was connected to the home-made high pressure optical cell by a thick-walled flexible capillary tube made of beryllium copper. A quartz sample cell, open to the helium gas, was installed inside the high-pressure optical cell. The high-pressure cell with three sapphire windows was placed in a special cryostat with a precise temperature control (UTREX, Ukraine). The cell was cooled by helium vapour or liquid helium surrounding the cell, depending on temperature desired. The gas pressure inside the cell was measured with a manganin gauge up to the freezing point of helium at a given temperature. The pressure of solidified helium in the cell was estimated from the computed and tabulated data for thermodynamic properties of ^{4}He [25].

Enough time was left between the pressure change and the measurement to reach the equilibrium temperature and pressure. Reversibility of the pressure-induced effects at a fixed temperature was checked by comparison of the data recorded along two experimental paths: in the course of compression and decompression.

2.3. Spectral and kinetic measurements

The excitation source was the Coherent 700 styryl-9M mode-locked dye laser synchronously pumped at 76 MHz by the Coherent Antares 76S Nd:YAG laser. To realise the ZnP excitation at 424 nm the output of the dye laser was frequency-doubled by using the $LiIO_3$ crystal. The time-resolved emission spectrum was recorded through a subtractive-dispersion double grating monochromator, put together from two single grating monochromators (LOMO, Russian Federation), with 2 nm spectral bandwidth by using the Hamamatsu C1587 Temporal Photometer in the synchroscan mode. The streak camera was linked via a vidicon to the OSA 500 optical multichannel analyser (B&M Spektronik, FRG). With a 3–5 ps dye laser pulsewidth, the temporal response function of the whole instrument was about 15 ps (FWHM). For more details about spectrally-limited picosecond time-resolved emission spectroscopy, see [26]. A polariser at the magic angle (54.7°) to exclude the rotational diffusion effects on the fluorescence decay kinetics at room temperature was routinely used.

The steady-state fluorescence emission spectra

were recorded with 1 nm bandwidth. Absorption spectra were measured by a Beckman Acta MVII spectrophotometer equipped with a special holder for placing the high-pressure cell, applying 1 nm bandwidth.

Care was taken to avoid sample degradation or multiple excitation effects due to excess light intensity. In the case of the ZnP–PM complex, no degradation was observed at excitation intensities ≤ 20 mW/cm^2. The proteins withstand almost 10 times higher intensity, ≤ 150 mW/cm^2. Absorption spectra at room temperature were run before and after each set of kinetics experiments to verify that the sample was not degraded during the measurement.

2.4. Data handling

The data were transferred to IBM Pentium PC and handled by utilising the Spectra Solve software (LasTek, Australia). The emission spectra were corrected for the spectral sensitivity of the setup. The peak energies and bandwidths of the steady-state and time-resolved spectra were obtained by fitting to the Gaussian lineshape. Global as well as single-curve analysis of the emission kinetics was performed. Lifetimes were calculated using a least-squares fitting algorithm assuming multiexponential kinetics and taking into account the finite instrument response function. Excitation pulses scattered from the sample were utilised as the instrument response function. The time-resolved fluorescence emission spectra at fixed pressure and temperature were constructed as

$$I(\lambda,t) = \sum A_i(\lambda) \exp(-t/\tau_i) \quad (2)$$

where the sum was over the number of kinetics components, with the initial amplitude A_i, used in the fitting procedure. Note that the components with negative pre-exponential factors belong to the rising parts of kinetics.

3. Results

3.1. ZnP–PM steady-state fluorescence emission spectra under pressure at room temperature

Fig. 2 shows the fluorescence emission spectra of the ZnP–PM complex in the 580–720 nm region,

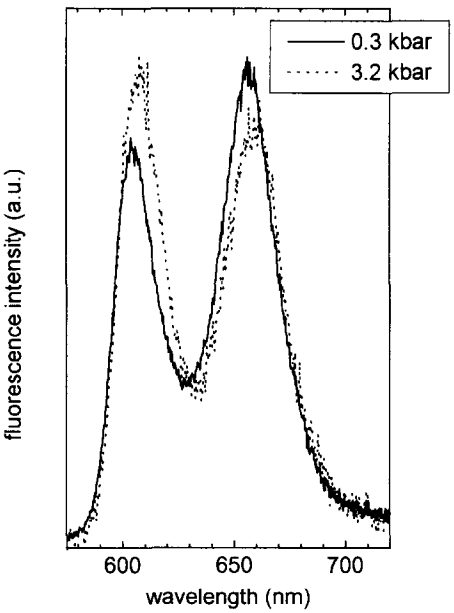

Fig. 2. Room-temperature steady-state fluorescence emission spectra of the ZnP–PM complex at 0.3 and 3.2 kbar. The spectra are normalised to the same maximal intensity.

measured at 0.3 and 3.2 kbar external pressure. The excitation was into the strong Soret absorption band at about 424 nm (here and below the specific numbers are given at 1 atm, if not indicated otherwise). The excitation wavelength was adjusted when pressure was changed in order to always hit the peak of the absorption band. Pumping to the weak 555 nm Q absorption band gave almost identical results. This is in agreement with the known fast internal conversion of high energy singlet excited states into the lowest energy Q vibronic manifold present in many porphyrin molecules [27]. The spectrum in Fig. 2, consisting of two major bands, looks like a typical emission spectrum of metalloporphyrins. Accordingly, the band at 602 nm may be classified as the $Q_x(0,0)$ origin band and the one at 655 nm, as its $Q_x(0,1)$ vibronic satellite [27].

The emission spectrum shifts linearly to the red when pressure is raised. The rate of the shift is essentially equal for both emission bands and tells for the dispersion origin of the shift. The shift data are in agreement with earlier observations for some other metalloporphyrins [28,29]. The common nature of the (0,0) band in the emission and absorption

spectra is validated by the same pressure-induced shift at the approximate rate of $-24\ cm^{-1}$/kbar.

Pressure also causes a small intensity redistribution between the vibronic bands, providing evidence of a decreasing intramolecular vibronic coupling with pressure. This may be a result of the conformational distortion of the porphyrin macrocycle by compression. It has been observed that structural perturbations alter several photophysical properties of porphyrins [30].

3.2. Pressure dependence of the ZnP–PM emission kinetics

The similarity of the steady-state spectra of the ZnP–PM complex and the spectra of metalloporphyrins without attached acceptor groups implies only a weak perturbation of the ZnP valence electrons by the presence of the PM acceptor. It also suggests that excitation is at least initially predominantly localised on the donor part of the donor–acceptor complex. At the same time, the emission intensity of the ZnP–PM complex is strongly quenched and its lifetime shortened as compared to the closed shell metal (Zn, Mg) metalloporphyrins [27,31]. Usually, decay times in the nanosecond range have been recorded in various solvents at 1 atm [27,31] and under high pressure, similar to the pressures applied in the present work [28,29].

As shown in Fig. 3, we have observed only about 70 ps excited state lifetime at normal pressure. This lifetime agrees well with the time constant for formation of the ZnP^{+}–PM^{-} charge transfer state measured by transient absorption (S. Millen and M.R. Wasielewski, unpublished result). Under these circumstances, one can write

$$\tau_{obs} = (k_R + k_{NR} + k_{ET})^{-1} \approx k_{ET}^{-1} \qquad (3)$$

where τ_{obs} is the observed fluorescence emission lifetime and k_R, k_{NR}, and k_{ET} are, respectively, the radiative, nonradiative (intersystem crossing plus internal conversion), and ET deactivation rates of the ZnP excited Q state. Eq. (3) allows a straightforward determination of the photoexcited ET rate and its pressure dependence in the ZnP–PM complex, by measuring ZnP emission kinetics after picosecond pulse excitation at various pressures.

Fig. 3 shows the pressure-dependent fluorescence kinetics recorded at the maximum of the $Q_x(0,0)$ emission band. At all pressures, the observed kinetics can be fitted to two decaying exponentials with the major fast and the minor slow components. At 1 atm, the following decay constants were observed: $\tau_1 = 73 \pm 3$ ps and $\tau_2 = 1530 \pm 120$ ps with $A_1/A_2 \geq 10 \pm 2$ (see Eq. (2)). Within the limits of error, there is no wavelength dependence of the kinetics over the emission band.

The pressure dependence of τ_1 is rather unusual. The decay time of 73 ps at 1 atm first decreases down to the minimum value of 47 ps at about 2 kbar. At higher pressures the lifetime increases gradually. However, this increase is much slower than the initial decrease. The initial normal-pressure value of τ_1 is recovered only at about 8 kbar. The reciprocals of τ_1 are plotted in Fig. 4. τ_2 also decreases with pressure, but only until 2 kbar where the lifetime 700 ± 150 ps was observed. At higher pressures this value did not change any more. It should be emphasised that all these pressure effects are perfectly

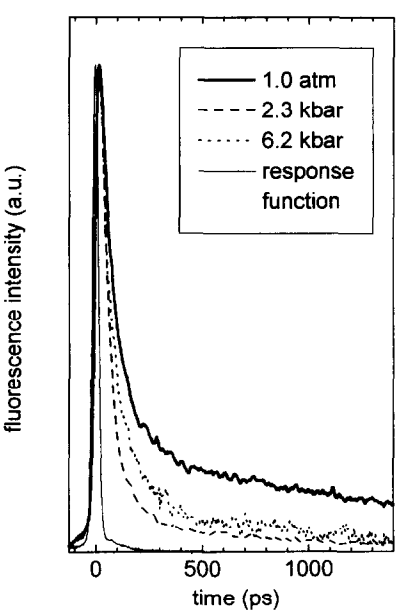

Fig. 3. Fluorescence emission kinetics of the ZnP–PM complex recorded at the $Q_x(0,0)$ emission band maximum under various pressures at room temperature. The curves are normalised to the same maximal intensity. The instrument response function is shown by thin solid line.

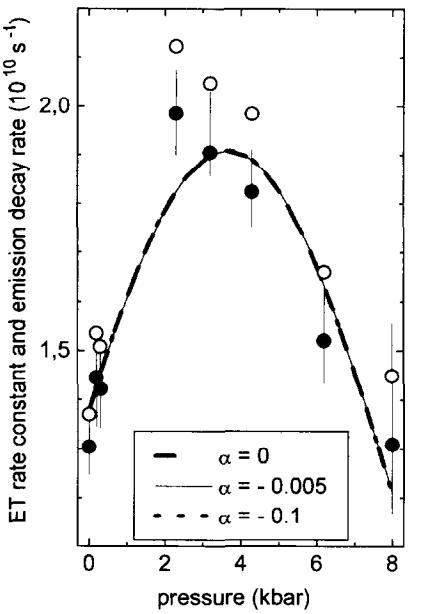

Fig. 4. Plots of the experimental emission decay rates τ_1^{-1} (open circles) and electron transfer rate constants k_{ET} (filled circles) against pressure in the ZnP–PM complex at room temperature. Different curves are least-squares fits of Eq. (16) (Model I) to the experimental data. Fit parameters are collected to Table 1.

reversible in the studied 1 atm–8 kbar pressure range.

3.3. Conformational high pressure effects in FMO protein trimers, as reflected by emission spectra and kinetics

In the glassy state at low temperatures, the protein characteristics depend on prehistory, i.e. on the sequence in which the sample is pressurised and cooled [21]. The dependence of the FMO protein emission spectrum on the way of the sample preparation is demonstrated in Fig. 5a. When the sample was first cooled and then pressurised (hereafter, cooling–and–pressurising (C/P) pathway), the shape of the spectrum did not change compared to the reference (R) spectrum, except for a moderate broadening. The most prominent pressure effect in this case was a red-shift of the spectrum from 827 nm to 833 nm (by 87 cm^{-1}). In the case of the P/C route, i.e. when the pressure was applied prior to cooling, the major effect was a much stronger broadening and essential loss of the spectral structure. The red-shift, although present, was less pronounced than in the C/P case. The emission kinetics (Fig. 5b) fastened markedly in the P/C case, whereas only slight changes were seen when the C/P route was used.

The experiments described give evidence that essential changes of the protein structure take place, if high pressure of the helium gas was applied at room temperature (for some more details, see [32]). This is in striking contrast to the case when pressure was applied at low temperature to the frozen protein solution. Then the pressure effects are similar to more conventional molecular solids, including crystals.

Considering profound changes, after the P/C cycle, of the low-temperature emission spectrum, extensive conformational distortions probably take place on the level of protein tertiary and quaternary structure. Some of the pressure effects, if pressure was applied at room temperature, may be connected with high solubility of helium gas in flexible protein structure. However, there is an evidence (A. Ellervee et al., unpublished data) that pressures up to 2.3 kbar applied at room temperature do not deteriorate the low-temperature structure of the absorption spectrum.

In order to avoid complications connected with these unsolved conformational effects, the high-pressure experiments described in Section 3.4 were performed in the C/P mode.

3.4. Transient exciton emission spectra of the FMO protein below 100 K as a function of pressure and temperature

In the low-temperature absorption spectrum (not shown) of the FMO protein from *C. tepidum*, there are three distinct maxima at about 805, 815, and 825 nm. At temperatures below 20 K, the steady-state emission spectrum is resonant to the lowest energy 825 nm absorption band. At higher temperatures (20 $K \leq T \leq 150$ K), an additional emission structure, resonant to the 815 and 805 nm absorption bands, appears. It has been proven by a simple Boltzmann factor analysis [16,33] that this anti-Stokes structure is due to equilibrium population of the FMO monomer subunit exciton states absorbing at 815 and 805 nm.

The normal-pressure FMO exciton emission kinetics excited at 805 nm (excitation bandwidth 4 nm) and recorded at four different wavelengths at 6 K is shown in Fig. 6. The kinetics is not single-exponential and can be fitted by a sum of three decaying and one rising exponential components having different amplitudes at different recording wavelengths. The shortest decay constant varies between 7 ps and 60 ps, whereas the two longer ones are about 200 ps and 2 ns. The emission rise time constant (evident at longer wavelengths) is between 10 ps and 30 ps.

Fig. 7 reproduces the normal-pressure transient emission spectra at 6 K. The spectra are constructed from spectrally selective kinetics accoding to the procedure described in Section 2.4 (see also [17]). For comparison, a steady-state emission spectrum is also shown in the upper part of Fig. 7.

As appears in Fig. 7, the transient emission spectrum at 'zero' delay peaks at about 823 nm. This is four nanometres to the blue compared to the maximum of the steady-state emission spectrum at 827 nm. Seen is also a weak signal around 815 nm, representing small nonequilibrium population of excitons in that state. The small intensity of the 815 nm emission band verifies ultrafast inter-exciton state relaxation revealed by femtosecond pump-probe and photon echo spectroscopies [17,34,35]. It also indicates that in the present experimental conditions (low temperature, excitation at 805 nm with a few picosecond long pump pulses), the upper exciton states depopulate almost completely during excitation pulse and excitons accumulate at the states close to exciton band bottom. The evolution of the 823 nm 'zero'-time spectrum includes a red-shift, gain in intensity, and broadening. These changes occur within about 80–100 ps, after which both the peak position and bandwidth acquire equilibrium value. Subsequent emission intensity decrease is due to finite exciton lifetime (characterised by 2–3 ns time constant).

The temperature dependence of the dynamic spectral red-shift is demonstrated in Fig. 8. A gradual reduction of the overall shift with temperature is observed. At 80 K the peak position appears practically time-independent (within about 5 cm^{-1} experimental uncertainty). It is also evident from Fig. 8 that while the initial (1 ps) peak position undergoes a red-shift, the nanosecond (equilibrium) peak position reveals an opposite blue-shift. The increase in the initial shift with increasing temperature is presumably related to the enhanced relaxation rate at higher

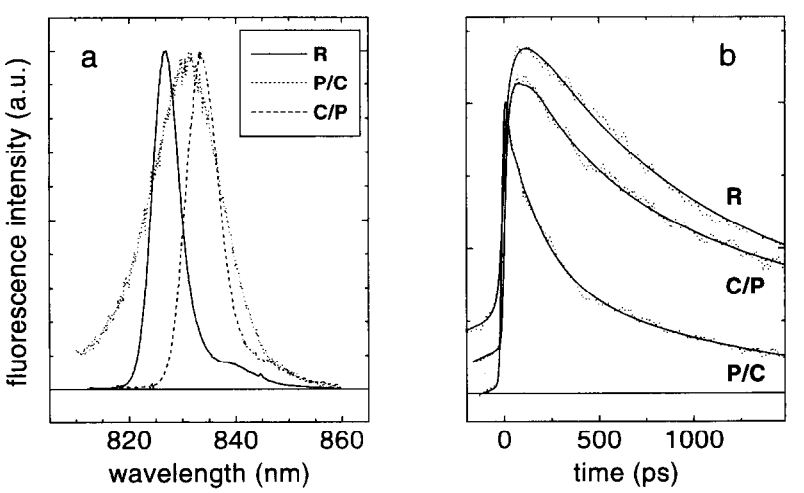

Fig. 5. (a) Exciton emission spectra (excitation at 805 nm, recording bandwidth 2 nm) of the FMO protein at 20 K and 6.5 kbar after different cooling (C) and pressurising (P) pathways. A reference spectrum (R) at 20 K and 1 atm is also shown. (b) The emission kinetics at 20 K (dots) together with the fitting functions (solid curves). The parameters of the fitting function (see Eq. (1)) are as follows. For R (p = 1 atm, recording wavelength 827 nm): τ_1 = 560 ps, A_1 = 16; τ_2 = 1440 ps, A_2 = 84; τ_3 = 20 ps, A_3 = −84. For C/P (p = 6.5 kbar, 833 nm): τ_1 = 160 ps, A_1 = 32; τ_2 = 1490 ps, A_2 = 68; τ_3 = 25 ps, A_3 = −68. For P/C (p = 6.0 kbar, 832 nm): τ_1 = 30 ps, A_1 = 34; τ_2 = 190 ps, A_2 = 38; τ_3 = 1380 ps, A_3 = 28.

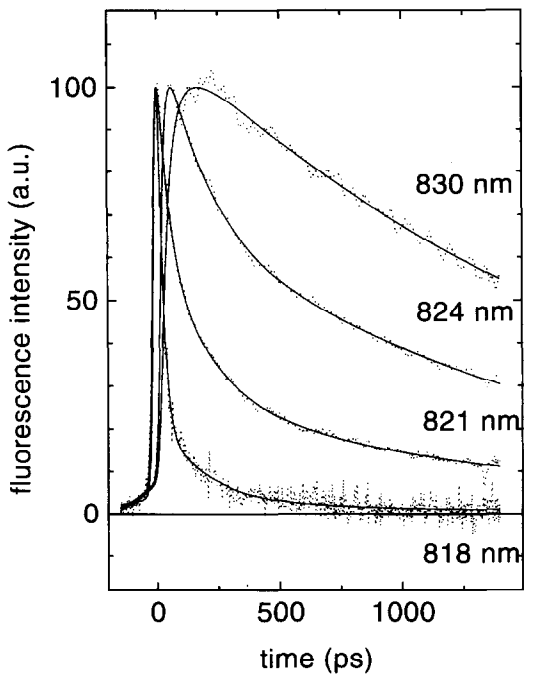

Fig. 6. Normalised exciton emission kinetics (dots) of the FMO protein measured at different wavelengths (recording bandwidth 2 nm) together with the fitting functions (solid curves). Excitation at 805 nm, $T = 6$ K, $p = 1$ atm. The fitting function (see text) parameters are as follows. For recording at 818 nm: $\tau_1 = 17$ ps (amplitude 1.00), $\tau_2 = 204$ ps (0.03), and $\tau_3 = 1850$ ps (0.01). For 821 nm: $\tau_1 = 45$ ps (3.16), $\tau_2 = 205$ ps (1.57), $\tau_3 = 1920$ ps (1.00), and $\tau_4 = 8$ ps (-1.00). For 824 nm: $\tau_2 = 165$ ps (0.74), $\tau_3 = 1730$ ps (1.00), and $\tau_4 = 9$ ps (-1.00). For 830 nm: $\tau_3 = 2040$ ps (1.00) and $\tau_4 = 29$ ps (-1.00).

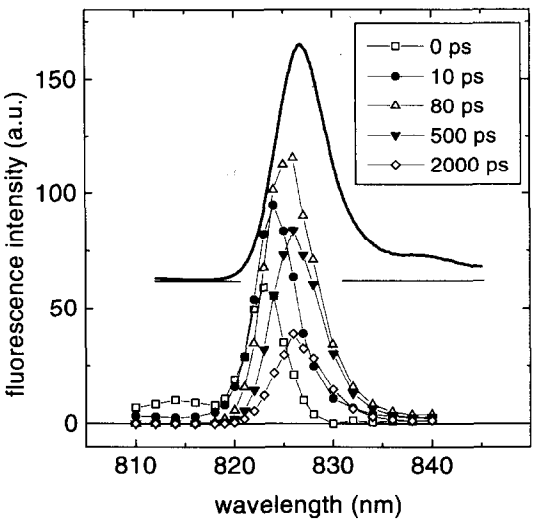

Fig. 7. Transient emission spectra of the FMO protein ($T = 6$ K, $p = 1$ atm) at different picosecond delay times (points). The spectra are constructed as described in the experimental section. For comparison, the steady-state emission spectrum is shown (thick solid curve). In both cases, excitation at 805 nm was used.

temperatures. A blue-shift of the equilibrium band maximum is most probably due to exciton-phonon coupling and has been known before [16,33].

The influence of sample compression on the dynamic band-shift at 20 K is shown in Fig. 9. It can be seen that the overall shift becomes about 15% smaller when pressure is increased up to 6 kbar.

For the sake of some unified comparison of the dynamics at various temperatures and pressures, we will take advantage of dielectric response theories (see, e.g., [23]) and introduce a normalised response function as follows

$$S_\nu(t,\Delta) = [\nu(t) - \nu(\infty)]/[\nu(\Delta) - \nu(\infty)] \quad (4)$$

Within the linear response limit, the solvation dynamics is completely characterised by Eq. (4). In Eq.

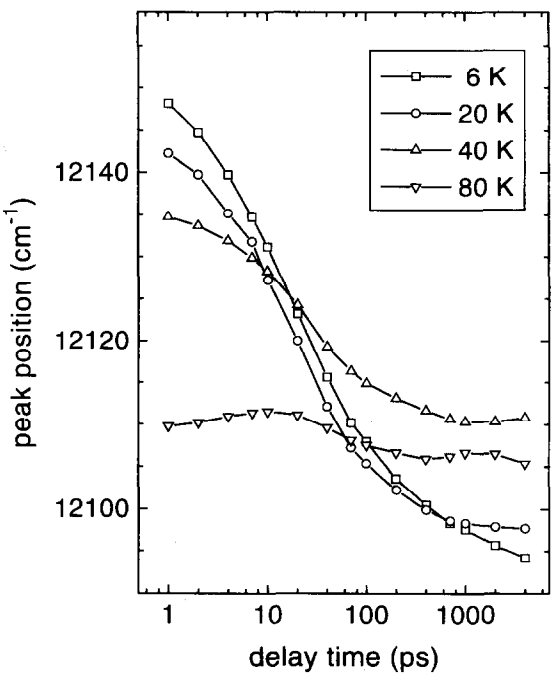

Fig. 8. Time dependence of the exciton emission peak energy of the FMO protein at different temperatures and $p = 1$ atm (points). Solid curves connecting experimental points serve merely as guides for the eye. Note the logarithmic time-scale.

(4), $\nu(t)$ is the emission peak energy at time t, Δ is the experimental time resolution, $\nu(\Delta)$ and $\nu(\infty)$ are, respectively, the initial and equilibrated peak positions, averaged over the instrument response function.

Function $S_\nu(t, \Delta)$, calculated at different temperatures and pressures, is shown in Fig. 10. Note the time axis spanning almost four decades, from 1 ps (an instrument-limited value) to almost 10 ns (an excited state lifetime-limited value). During this time, the maximum of the emission spectrum at 6 K shifts toward lower energy by 57 cm^{-1}. About 2/3 of the total shift occurs within first 50 ps past excitation. Yet almost two orders of magnitude longer time is needed to cover the remaining 1/3 of the shift. Fitting to the sum of decaying exponentials reveals four time constants at 6 K, each in a different decade: 5.4 ± 1.3 ps (the corresponding shift is 15 cm^{-1}), 26 ± 7 ps (23 cm^{-1}), 163 ± 58 ps (12 cm^{-1}), and 1930 ± 590 ps (7 cm^{-1}). An average time constant, calculated as $\tau_{av} = (\Sigma A_i \tau_i)/\Sigma A_i$ (A_i stands for the shift connected to the decay constant τ_i), is 283 ± 88 ps.

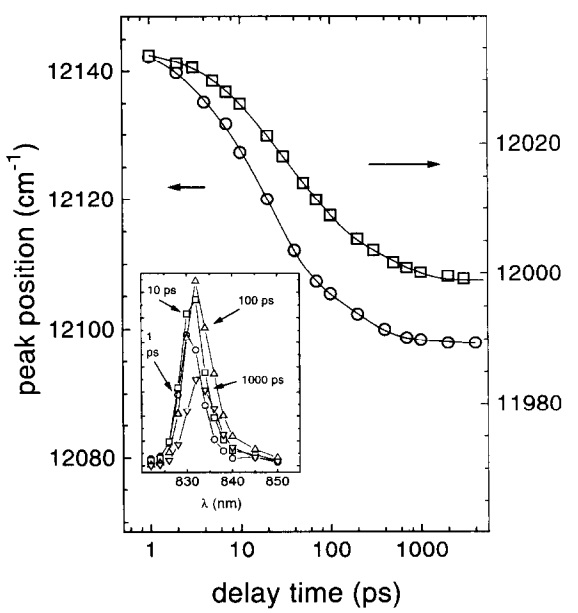

Fig. 9. Time dependence of the exciton emission peak energy of the FMO protein at 20 K and two pressures: 1 atm (circles) and 6 kbar (squares). Note the shifted y-axis origin of the different data sets. Solid curves are only guides for the eye. Insert: the transient emission spectra at 1 atm and different picosecond delay times indicated.

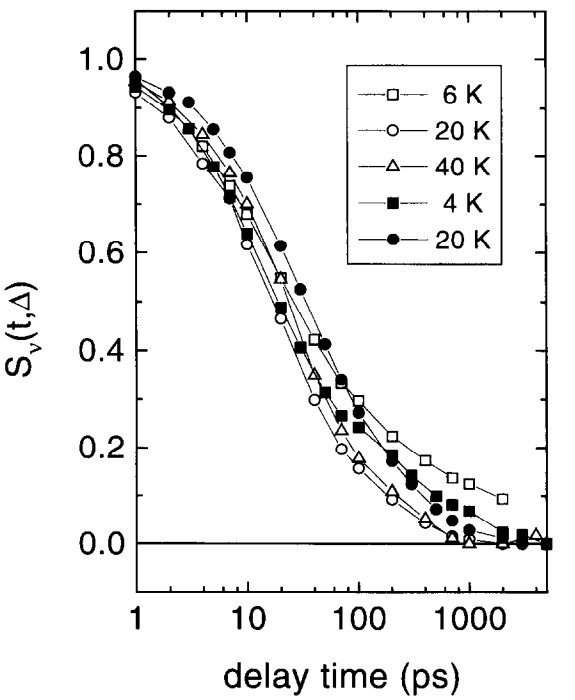

Fig. 10. Normalised response function $S_\nu(t, \Delta)$, calculated from the exciton emission band shift dynamics data at various temperatures and different pressures (open symbols, at 1 atm; filled symbols, at 6 kbar) as described in the text. The multiexponential fitting function (solid lines) parameters are discussed in the text.

Some fastening of the dynamics with temperature can be seen in the normalised scale of Fig. 10, in agreement with the notion made above. However, virtually no change of the dynamic response with pressure is observed at fixed temperature. The pressure-insensitivity of the ultrafast exciton dynamics in the FMO protein has been pointed out earlier [20] and argued to be a consequence of the linear pressure shifts being dominated by dispersion coupling.

4. Discussion

4.1. Pressure-dependent electron transfer model

By analogy with chemical reactions, the thermally activated ET rate constant in the high temperature

limit ($k_BT > h\nu$, for all relevant vibrations ν) can be expressed by an Arrhenius law [36]:

$$k_{ET} = \sqrt{\frac{4\pi^3}{h^2 E_r k_B T}}\,|V|^2 \exp(-G^+/k_B T) \qquad (5)$$

where G^+, the free energy of activation, is given by

$$G^+ = (E_r + E_g)^2/4E_r \qquad (6)$$

In Eqs. (5) and (6), h is the Planck's constant, k_B is the Boltzmann's constant, T is the temperature, E_g is the free energy gap, i.e. the energy difference between the minima of the free energy parabolas for the products and reactants (see Fig. 11 for the applied notation), or the reaction driving force, E_r is the reorganisation free energy of the solvent in the presence of reactants and products, V is the electronic coupling matrix element between initial and final states.

Eq. (5) and Fig. 11 represent the physical situation in the nonadiabatic weak coupling limit, which is valid in many cases. In this limit, the ET (and not the nuclear relaxation) is a rate-limiting process, proceeding slowly at the crossing point of the reactant and product potential energy surfaces. The ET rate explicitly depends only upon solvent energetics and not upon solvent dynamics.

Another extreme is the adiabatic process being almost independent of the electronic coupling strength. According to this view, the electronic coupling required for ET is large and the reaction rate is limited by the time required to achieve the proper nuclear configuration for an isoenergetic ET to occur. In this limit, $k_{ET} \propto \langle \tau_L \rangle^{-1}$, where $\langle \tau_L \rangle$ is the average solvation time.

Following [37,38], distinction between adiabatic and nonadiabatic reaction can be made by comparing V either with thermal energy, k_BT, or with $\langle \tau_L \rangle^{-1}$. Note that $\langle \tau_L \rangle^{-1}$ is a measure of the energy uncertainty of the reaction co-ordinate. Reaction is adiabatic, if $V \gg k_BT$ or $V > \langle \tau_L \rangle^{-1}$ and nonadiabatic, if $V \ll k_BT$ or $V < \langle \tau_L \rangle^{-1}$.

To the best of our knowledge, existing ET theories do not consider pressure effects. Yet, a general discussion in [39], based on the theory of optical transitions under pressure by Drickamer and Frank [40], should be acknowledged (see also [41] for

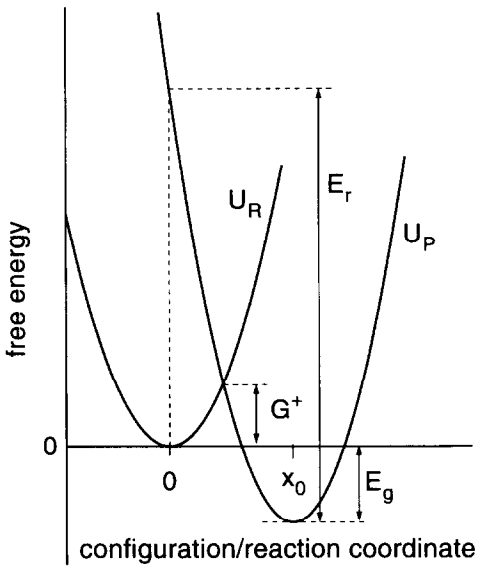

Fig. 11. Single configuration coordinate model of electron transfer. Note that here the free energy gap E_g is negative, since it is defined as the energy difference, $U_P(x_0) - U_R(0) < 0$, between the minima of parabolas for the final (product) and initial (reactant) states.

pressure effects on nonradiative transitions in molecular vibronic spectra). According to [39], the total pressure dependence of the ET rate constant can be represented by

$$\partial \ln k_{ET}/\partial p = \partial \ln|V|^2/\partial p + \partial \ln F/\partial p \qquad (7)$$

where F is the thermally averaged nuclear overlap factor. Compression will enhance the electronic coupling as

$$\partial \ln|V|^2/\partial p \propto \beta \kappa_T R \qquad (8)$$

where β is the scaling constant (see below), κ_T is the compressibility of the intervening bulk medium, and R is the donor–acceptor spacing.

By analogy with the theory of optical transitions [40], we suppose that the effect of external hydrostatic pressure on the reactant and product free energy surfaces ($U_R(x)$ and $U_P(x)$, respectively, in Fig. 11) can be described by adding the same pressure–volume work term, px, to both potentials. Let us further assume that the potentials are harmonic and coupled by a single configuration coordinate x which can be related to an effective vibrational mode. Then

the potential free energies upon application of pressure are:

$$U_R(x) = (1/2)k_R x^2 + px \quad (9)$$

$$U_P(x) = (1/2)k_P(x - x_0)^2 + E_g + px \quad (10)$$

In Eqs. (9) and (10), x_0 is the displacement of the free energy minima along x, and k_R and k_P are the force constants that characterise the steepness of the reactant and product free energy parabolas, respectively. In general, the force constants may be different for the reactant and product potential wells.

From the configuration coordinate diagram of Fig. 11, one can obtain the expression for the pressure dependence of the free energy gap:

$$E_g(p) = E_g(0) + x_0 p + \frac{1}{2}\left(k_R^{-1} - k_P^{-1}\right)p^2 \quad (11)$$

where $E_g(0)$ is the zero-pressure value. The pressure variation of the free energy gap is determined by the linear term with respect to pressure, which is due to the horizontal displacement of the potential energy minima, and by the term quadratic in pressure, which is absent if the force constants do not change at ET.

From Fig. 11, it also follows that

$$x_0(p) = x_0(0) + \left(k_R^{-1} - k_P^{-1}\right)p \quad (12)$$

where $x_0(0)$ is the zero-pressure displacement. The effective nuclear displacement x_0 at ET is seen to be pressure-sensitive only if the reactant and product potentials are characterised by different force constants. Note that, the force constants themselves, and thus vibrational frequencies, are considered independent of pressure [40].

The reorganisation free energy characterises the coupling strength between the electronic and nuclear degrees of freedom at ET. It is defined via x_0 and k_P as (see Fig. 11)

$$E_r = x_0^2 k_P/2 \quad (13)$$

$E_r \equiv 0$, if $x_0 = 0$. From Eqs. (12) and (13) one gets

$$E_r(p) = \left[x_0^2(0) + 2x_0(0)\left(k_R^{-1} - k_P^{-1}\right)p + \left(k_R^{-1} - k_P^{-1}\right)^2 p^2\right]k_P/2 \quad (14)$$

Note that as long as $k_R \neq k_P$, $E_r(p) \neq 0$ at $p > 0$, even if $x_0(0) = 0$.

4.2. Model calculations of the pressure dependence of the ET rate

The most impressive experimental result of the first part of this study is the observation of the inverted parabola-like dependence of τ_1^{-1} on applied pressure (Fig. 4). Inspection of Eqs. (7) and (8) assures that this cannot be explained by the electronic coupling term, thus underlining the decisive role of the nuclear coupling term.

In the following, an attempt shall be made to describe the pressure dependence of the photoinduced ET rate in the ZnP–PM complex based on the weak coupling model, outlined in the previous section. It is assumed that the reactant state in Fig. 11 corresponds to the state with locally excited ZnP molecule and the product state, to the ZnP^+PM^- charge-separated state. The locally excited state is reached by electronic transition from the ground state of the donor–acceptor complex. Coupling between the locally excited state and the charge-separated state is considered weak. Model parameters (free energy gap, reorganisation energy, and donor–acceptor separation) are supposed to be only linear functions of pressure, possible higher order terms are ignored. The ET rate constants have been evaluated from the experimental data as

$$k_{ET}(p) = \tau_1^{-1}(p) - \tau_2^{-1}(p) \quad (15)$$

where τ_1 and τ_2 are, respectively, the experimentally measured short and long lifetimes. By this procedure, we have implicitly assumed that τ_2 is the excited state lifetime of the ZnP–PM complex, if the ET is by some reason excluded.

4.2.1. Model I (reaction driving force is pressure-dependent)

Let us first consider the simplest model where E_g (along with R) depends linearly on pressure and E_r is constant. By modifying Eq. (5), we get:

$$k_{ET}(P) = \sqrt{\frac{4\pi^3}{h^2 E_r k_B T}}\,|V_0|^2 \exp(-\beta\alpha p) \times \exp\left(\frac{-\left(E_g(0) + \chi p + E_r\right)^2}{4E_r k_B T}\right) \quad (16)$$

Table 1
The fitting curve parameters in Fig. 4 based on Eq. (16)

	Solid curve	Dashed curve	Dotted curve
V_0 (cm^{-1})	5.03	4.64	5.32
α (nm/kbar)	−0.005 (fixed)	0 (fixed)	−0.1 (fixed)
$E_g(0)$ (cm^{-1})	−1467	−1112	−1362
χ (cm^{-1}/kbar)	140	117	−190
E_r (cm^{-1})	966	683	1782

Here, the commonly used exponential form for the distance dependence of the electronic coupling matrix element has been accepted [42]:

$$V = V_0 \exp[-\beta(R - R_0)/2] \quad (17)$$

V_0 and R_0 are, respectively, the electronic coupling strength and donor–acceptor distance at 1 atm, χ is the rate of the change of the free energy gap with pressure, $\Delta E_g/p$, and $\alpha = (R - R_0)/p$ (for simplicity, the normal pressure value is taken zero, so that $\Delta p \approx p$). For $R_0 \approx 0.5$ nm, $\alpha \approx -0.005$ nm/kbar, if the volume compressibility is 0.03 $kbar^{-1}$, a value rather typical for the condensed molecular matter [19].

Fig. 4 and Table 1 show the results of the least-squares fit with α and β (≈ 7 nm^{-1} [42]) as fixed parameters. As seen in Fig. 4, the modified Marcus formula, Eq. (16), that takes into account a linear pressure dependence of the free energy gap, successfully reproduces the inverted parabola-like pressure dependence of the ET rate constant. Fig. 4 also shows that the pressure dependence of the electronic coupling matrix element due to pressure variation of R in Eq. (16) has practically no influence on the overall ET rate. Considering the higher stiffness of the ZnP–PM covalent bond as compared to molecular solids, this conclusion is even more justified.

It is important to note that the least-squares fitting parameters $E_g(0)$ and $E_r(0)$ in the first and second column of Table 1 look quite reasonable. From the independent source [1], it is known that $E_g(0) \approx -1600$ cm^{-1} and $E_r(0) \leq 800$ cm^{-1}. Also the χ value is rational. Its positive sign means that $-E_g$ is getting smaller along with the pressure increase. If $-\alpha$ is taken nonphysically large (last column of Table 1), the other parameters become unreasonable too.

Fulfilment of the criterion $V \ll k_B T$ ($V_0 \approx 5$ cm^{-1} from Table 1, $V \approx 6$ cm^{-1}, as calculated from Eq. (17) for $\alpha \approx -0.005$ nm/kbar and $p = 8$ kbar, whereas $k_B T \approx 205$ cm^{-1} at 295 K) suggests that the reaction under study can indeed be considered as nonadiabatic. For a double check, one needs to know the relaxation rate of the solvent polarisation fluctuations. Although the experimental data for toluene are not available, an estimate can be made based on Fig. 3 of Ref. [38]. It follows that toluene is a fast relaxing solvent with $\langle \tau_L \rangle^{-1} \approx 3 \cdot 10^{12}$ s^{-1}, that corresponds to the energy uncertainty of 100 cm^{-1}. Since dielectric properties of most organic liquids are known to change no more than 20% over the relevant pressure range [43], the same approximate value, 100 cm^{-1}, should be characteristic for toluene at high pressures used. Satisfaction of the inequality $V \ll \langle \tau_L \rangle^{-1}$ provides another support for the nonadiabatic ET.

Despite the success in explaining the main trend in the pressure dependence of the ET rate, Eq. (16) totally fails when the asymmetry of this dependence is considered. The fitting curves in Fig. 4 are fairly symmetric with respect to their maximum, whereas the experimental data show essential asymmetry. Therefore, further elaboration of the model is needed.

4.2.2. *Model II (reorganisation free energy is pressure-dependent)*

Here we assume that E_r (and also R) depends linearly on pressure whereas E_g is constant. According to Eq. (14), E_r depends on pressure, only if force constants (or, vibration frequencies) characterising the reactant and product states are different ($k_R \neq$

Table 2
The fitting curve parameters in Fig. 12 based on Eq. (18)

	Solid curve	Dotted curve	Dashed curve
V_0 (cm^{-1})	5.58	4.32	4.49
α (nm/kbar)	−0.005 (fixed)	−0.005 (fixed)	−0.005 (fixed)
E_g (cm^{-1})	−1509 (fixed)	−592	−629 (fixed)
$E_r(0)$ (cm^{-1})	845	209	209 (fixed)
δ (cm^{-1}/kbar)	165	88	103

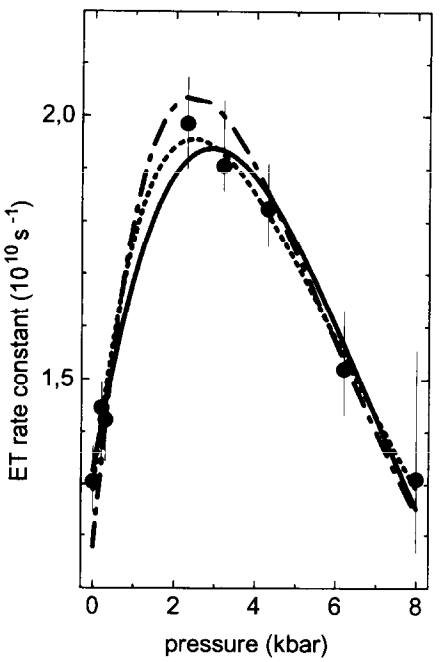

Fig. 12. Modelling (according to the Model II) of the ET rate as a function of applied pressure in the ZnP–PM complex. The fitting formula is Eq. (18) and the fit parameters are given in Table 2.

k_P). Note that the classical Marcus ET model [36] considers the case of identical reactant and product force constants. Our model II yields:

$$k_{ET}(p) = \sqrt{\frac{4\pi^3}{h^2(E_r(0)+\delta p)k_B T}}\,|V_0|^2 \times \exp(-\beta\alpha p)\exp\left(\frac{-(E_g+E_r(0)+\delta p)^2}{4(E_r(0)+\delta p)k_B T}\right) \quad (18)$$

where δ is the rate of the change of the reorganisation energy with pressure, $\Delta E_r/p$. Fig. 12 shows the result of the least-squares fit with different parameter sets collected into Table 2.

This model reproduces quite successfully both the inverted parabola-like curve as well as its asymmetry. The best fit is obtained when E_g is taken as the free parameter (see dotted curve in Fig. 12 and the second column in Table 2). However, in this case, the iterated E_g value is too small relative to its known value, about -1600 cm^{-1}. The positive sign of δ implies that E_r is increasing with pressure. It follows from Eq. (14) that in this case, $k_P > k_R$, and the product potential U_P appears to be sharper than the reactant potential U_R.

4.2.3. Model III (both the driving force and the reorganisation energy are pressure-dependent)

This is a combination of the previous two models where the free energy gap, solvent reorganisation energy, and donor–acceptor distance all change linearly with pressure. We have:

$$k_{ET}(p) = \sqrt{\frac{4\pi^3}{h^2(E_r+\delta p)k_B T}}\,|V_0|^2 \exp(-\beta\alpha p) \times \exp\left(\frac{-(E_g+\chi p+E_r+\delta p)^2}{4(E_r+\delta p)k_B T}\right) \quad (19)$$

The results of fitting based on Eq. (19) are shown in Fig. 13 and the relevant parameters are gathered into Table 3.

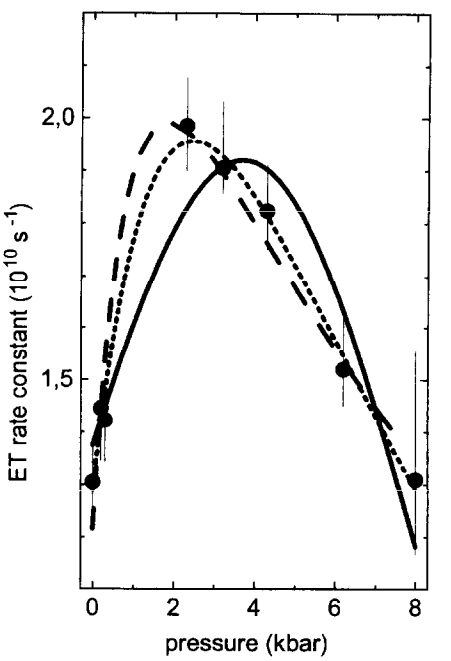

Fig. 13. The same as in Fig. 12, except that the fitting formula is Eq. (19) and the fit parameters are given in Table 3 (Model III).

Table 3
The fitting curve parameters in Fig. 13 based on Eq. (19)

	Solid curve	Dashed curve	Dotted curve
V_0 (cm^{-1})	5.06	6.70	6.25
α (nm/kbar)	−0.005 (fixed)	−0.005 (fixed)	−0.005 (fixed)
$E_g(0)$ (cm^{-1})	−1509 (fixed)	−1509 (fixed)	−1714
χ (cm^{-1}/kbar)	151 (fixed)	−503 (fixed)	−201
$E_r(0)$ (cm^{-1})	1003	687	913
δ (cm^{-1}/kbar)	−8	654	384

The parameter set in Table 3 (yielding the solid curve in Fig. 13) obviously does not fit well the experimental data. The other two sets give almost equally good result. To discriminate between them, more data points between 0 and 2 kbar are needed. From the physical point of view, perhaps, the dotted curve should be favoured.

In conclusion, a reversal of the sign of the derivative dk_{ET}/dp for the photoinduced ET rate has been observed. Taking into account the possibility that along with the driving force also the reorganisation energy is pressure-dependent (supposing that force constants change in ET) a consistent fit to the experiment is achieved. The applicability of the nonadiabatic ET model is well justified in the present case because V ($\approx$ 4–8 cm^{-1}) $\ll k_BT$ ($\approx$ 205 cm^{-1} at 295 K) and also $V \ll \langle \tau_L \rangle^{-1}$ ($\approx$ 100 cm^{-1} in toluene at 1 atm and 295 K).

4.3. Pico-nanosecond dynamics of the lowest energy (825 nm) FMO protein exciton emission band

As was described in Section 3.4 (see also [16,17]), there are dynamical processes in the FMO protein emission spectrum that develop on the time-scale long compared to the population relaxation time of the higher energy monomer exciton states grouped at 805 and 815 nm. After few picoseconds past the excitation pulse, essentially only the lowest energy 825 nm state remains populated at liquid helium temperatures. Thus, the observed low-temperature evolution of the emission spectrum reflects equilibration of excitons at the exciton band bottom region only.

There is both theoretical [14,15] and experimental [18,44] evidence that the 825 nm band is not elementary. The coupling of Bchls belonging to different monomer subunits of the FMO protein trimer leads to splitting of the intra-subunit exciton levels. The C_3 symmetry of the FMO trimer dictates that there are two degenerate in-plane states and a nondegenerate out-of-plane state. Model simulations [14] and [15] offer, respectively, a 2.3 nm and 0.4 nm splitting between the in-plane and out-of-plane transitions. Hole-burning spectra [18] refer to the states 3.7 nm apart (at 827.1 and 824.4 nm).

There is, however, a poor agreement between different sources considering transition intensities. According to [14], the higher energy out-of-plane transition is about six times stronger than the two lower energy in-plane transitions taken together. After [15], in contrast, the lowest energy in-plane transitions dominate (over 99.8% of the oscillator strength is associated with them). From the hole-burning spectra [18], it was concluded that the 824 and 827 nm levels carry comparable absorption intensities. Refs. [44] and [14] agree in that most of the 825 nm band absorption strength is concentrated in higher energy states, but disagree in symmetry of these states. According to polarised singlet-minus-triplet and linear dichroism spectroscopy data [44], the degenerate in-plane states should be placed at higher energy compared to the single out-of-plane state.

Accepting the exciton picture, the present transient emission data (Figs. 7–9) can be interpreted as providing additional support to the partially hidden exciton substructure of the 825 nm band. The 4 nm dynamic red-shift (from 823 to 827 nm) observed by us is close to both theoretically predicted [14] and experimentally found [18] trimer exciton splitting values, although for the FMO complex from different bacterium, *Prosthecochloris aestuarii*.

Radiative strength of the 823 and 827 nm transitions can presently be only roughly considered due to lack of reliable low-temperature emission quantum yield data. Assuming $\leq$ 10% emission quantum yield of the lower (827 nm) state [14], about equal nonradiative decay rate of exciton states, and the rate of inter-exciton relaxation (from 823 to 827 nm) of about $(50\ ps)^{-1}$, it is not difficult to estimate from our transient emission data (Fig. 7) that the radiative decay rate of the 823 nm state should be substantially higher than the rate of the 827 nm state. This conclusion strongly favours the results of Refs. [14,44] and apparently disagrees with Ref. [15].

There are still important questions which have been remained without answer in the given exciton framework. Why is relaxation between the trimer exciton levels (at 823 and 827 nm) so slow (taking, as shown above, tens and even hundreds of picoseconds) compared to subpicosecond relaxation between exciton bands, dominated by couplings within the monomer protein subunit (at 805, 815, and 825 nm) [17]? Why is relaxation dynamics strongly non-exponential?

Involvement of slow conformational motions of surrounding protein (protein solvation) has been proposed [17] to solve the above issues. Indeed, non-exponential dynamical response of condensed matter to external perturbation is a universal rather than a unique phenomenon. Physically, this is due to the presence of a heterogeneous distribution of independently (exponentially) relaxing mesoscopic regions (for a recent review, see [45]). Attempt was also made to associate the dynamic shift time constants (see Section 3.4) with some geometrical constraints in the system as follows: (i) The 5.4 ± 1.3 ps time constant was related to the solvation within the monomer protein subunit, superimposed on the Bchl exciton relaxation; (ii) The 26 ± 7 ps time constant was assigned to energy transfer between monomer subunits in the FMO trimer; (iii) The 163 ± 58 ps and 1930 ± 590 ps time constants were connected to the configuration relaxation in the protein trimer and in the whole system (including protein and its water-glycerol glass surroundings), respectively. However tempting this approach may seem, the possibility of picosecond solvation in proteins at low temperatures (below the glass transition temperature of protein and surrounding water-glycerol glass) still needs to be proved. Spectral diffusion in myoglobin and cytochrome *c* has been studied at liquid helium temperatures, but on a much longer time scale, ≥ 10 ns [46].

5. Summary

In the present work, a question has been addressed, how external high hydrostatic pressure affects the photoinduced intramolecular ET and ER processes. Unlike phenomena, as they are, have been studied in different systems: ET in an artificial supramolecular complex, ER in a natural photosynthetic antenna protein. Spectrally selective picosecond time-resolved emission technique has been used to detect pressure-induced changes in the systems.

The following general conclusions can be drawn from the ET study: (i) External pressure may serve as a potential and sensitive tool not only to study, but also to control and tune ET (more generally, elementary chemical) reactions in solvents; (ii) Depending on system parameters, pressure can either accelerate or decelerate the rate of ET (chemical) reactions; (iii) If competing pathways of the reaction are available, pressure can probably change the branching ratio between the pathways; (iv) Pressure effects are due to pressure dependence of the reaction driving force or/and reorganisation free energy.

The effect of pressure on the exciton relaxation dynamics in the FMO antenna protein turned out to be marginal. This may probably be explained by rather a unique structure of the FMO protein [11,12]. In each of the three subunits, the polypeptide backbone forms large β-sheets and encloses a central core of seven Bchl molecules. A barrel made of low compressibility β-sheets may, like a diving bell, effectively screen the inside Bchl molecules from external influence of high pressure. The origin of the observed slow (pico-subnanosecond) dynamics of the FMO excitons in the 825 nm state remains open. The phenomenon may be due to weak coupling of phonons to the trimer exciton states or/and to low density of the relevant low-frequency (≈ 50 cm^{-1}) phonons. Exciton solvation in the surrounding protein and water-glycerol matrix may also contribute to this effect.

Drastic changes of spectral, kinetic and dynamic properties have been observed due to protein denaturation, if the protein was compressed at room temperature and then cooled down, as compared to the samples, first cooled and then pressurised.

Acknowledgements

The authors are grateful to Drs. M. Miller and M. Wasielewski for kindly providing the samples. This work was supported by the International Science Foundation under the grants LCF 000 and LL3 100, by the Estonian Science Foundation under the grant

No. 2271, and by the Argonne National Laboratory under Contract (REP) No. 94-62JC-033.

References

[1] G.P. Wiederrecht, M.P. Niemczyk, W.A. Svec, M.R. Wasielewski, J. Am. Chem. Soc. 118 (1996) 81.
[2] R.E. Gibson, O.H. Loeffler, J. Am. Chem. Soc. 61 (1939) 2877.
[3] A.M. Rollinson, H.G. Drickamer, J. Chem. Phys. 73 (1980) 5981.
[4] D. Kleinfeld, in: B. Chance, D.C. de Vault, H. Frauenfelder, R.A. Marcus, J.R. Schrieffer, N. Sutin (Eds.), Tunneling in Biological Systems, Academic Press, New York, 1979, p. 384.
[5] C.W. Hoganson, M.W. Windsor, I. Farkas, W.W. Parson, Biochim. Biophys. Acta 892 (1987) 275.
[6] M.W. Windsor, R. Menzel, Chem. Phys. Lett. 164 (1989) 143.
[7] H. Lueck, M.W. Windsor, W. Rettig, J. Phys. Chem. 94 (1990) 4550.
[8] N.L. Redline, M.W. Windsor, R. Menzel, Chem. Phys. Lett. 186 (1991) 204.
[9] H.C. Chang, R. Jankowiak, N.R.S. Reddy, G.J. Small, Chem. Phys. 197 (1995) 307.
[10] R.E. Blankenship, J.M. Olson, M. Miller, in: R.E. Blankenship, M.T. Madigan, C.E. Bauer (Eds.), Anoxygenic Photosynthetic Bacteria, Kluwer Academic Publishers, Dordrecht, 1995, p. 399.
[11] D.E. Tronrud, M.F. Schmid, B.W. Matthews, J. Mol. Biol. 188 (1986) 443.
[12] Y.-F. Li, W. Zhou, E. Blankenship, J.P. Allen, J. Mol. Biol., submitted.
[13] K.D. Philipson, K. Sauer, Biochem. 11 (1972) 1880.
[14] R.M. Pearlstein, Photosynth. Res. 31 (1992) 213.
[15] D. Gülen, J. Phys. Chem. 100 (1996) 17683.
[16] A. Freiberg, P. Kukk, M. Tars, M. Miller, in: A. Tramer (Ed.), Fast Elementary Processes in Chemical and Biological Systems, American Institute of Physics Press, Woodbury, USA, 1996, p. 262.
[17] A. Freiberg, S. Lin, K. Timpmann, R.E. Blankenship, J. Phys. Chem., submitted.
[18] S. Johnson, G.J. Small, J. Phys. Chem. 95 (1991) 471.
[19] M. Tars, A. Ellervee, P. Kukk, A. Laisaar, A. Saarnak, A. Freiberg, Lithuanian J. Phys. 34 (1994) 320.
[20] N.R.S. Reddy, R. Jankowiak, G.J. Small, J. Phys. Chem. 99 (1995) 16168.
[21] H. Frauenfelder et al., J. Phys. Chem. 94 (1990) 1024.
[22] V. Mozhaev, K. Heremans, J. Frank, P. Masson, C. Balny, Proteins 24 (1996) 81.
[23] R.M. Stratt, M. Maroncelli, J. Phys. Chem. 100 (1996) 12981.
[24] M. Miller, R.P. Cox, J.M. Olson, Photosynth. Res. 41 (1994) 97.
[25] A. Driessen, E. van der Poll, I.F. Silvera, Phys. Rev. B33 (1986) 3269.
[26] A. Freiberg, P. Saari, IEEE J. Quant. Electr. 19 (1983) 622.
[27] M. Gouterman, in: D. Dolphin (Ed.) The Porphyrins, vol. 3, Academic Press, 1978, p. 1.
[28] T.G. Politis, H.G. Drickamer, J. Chem. Phys. 74 (1981) 263.
[29] T.G. Politis, H.G. Drickamer, J. Chem. Phys. 76 (1982) 285.
[30] N.C. Maiti, M. Ravikanth, J. Photochem. Photobiol. 101 (1996) 7.
[31] A.T. Gradyuskho, V.A. Mashenkov, A.N. Sevchenko, K.N. Solov'ev, M.P. Tsvirko, Dokl. Akad. Nauk SSSR 182 (1968) 64 (Sov. Phys. Dokl., 13 (1969) 869).
[32] A. Freiberg, A. Ellervee, A. Laisaar, M. Miller, M. Tars, K. Timpmann, in: K. Heremans (Ed.), High Pressure Research in the Biosciences and Biotechnology, Leuven University Press, Leuven, Belgium, 1997, p. 159.
[33] T. Swarthoff, J. Amesz, H.J. Kramer, C.P. Rijgersberg, Israel J. Chem. 21 (1981) 332.
[34] R.J.W. Louwe, T.J. Aartsma, J. Lumin. 58 (1994) 154.
[35] S. Savikhin, W. Struve, Photosynth. Res. 48 (1996) 271.
[36] R.A. Marcus, J. Chem. Phys. 24 (1956) 966.
[37] Z. Wang, J. Tang, J.R. Norris, J. Chem. Phys. 97 (1992) 7251.
[38] C. Fuchs, M. Schreiber, J. Chem. Phys. 105 (1996) 1021.
[39] J. Jortner, Biochim. Biophys. Acta 594 (1980) 193.
[40] H.G. Drickamer, C.W. Frank, Electronic Transitions and the High Pressure Chemistry and Physics of Solids, Chapman & Hall, London, 1973.
[41] S.H. Lin, J. Chem. Phys. 59 (1973) 4458.
[42] C.C. Moser, J.M. Keske, K. Warncke, R.S. Farid, P.L. Dutton, Nature 355 (1992) 796.
[43] S.D. Hamann, Physico-Chemical Effects of Pressure, Butterworths, London, 1957.
[44] F. van Mourik, R.R. Verwijst, J.M. Mulder, R. van Grondelle, J. Phys. Chem. 98 (1994) 10307.
[45] R.V. Chamberlin, in: D.V. Hone (Ed.), 35 Years of Condensed Matter and Related Physics, World Scientific, 1996, p. 66.
[46] D.T. Leeson, D.A. Wiersma, Phys. Rev. Lett. 74 (1995) 2138.